Trends in Downwelling Longwave Radiance over the Southern Great Plains

Lei Liu[1], Yi Huang[1], John R. Gyakum[1], David D. Turner[2], P. Jonathan Gero[3]

[1]Department of Atmospheric and Oceanic Sciences, McGill University, Quebec, Canada.

[2]NOAA/OAR/Global Systems Laboratory, Boulder, Colorado, USA.

[3]Space Science and Engineering Center, University of Wisconsin-Madison, Madison, Wisconsin, USA.

Corresponding author: Lei Liu (lei.liu5@mail.mcgill.ca)

Key Points:

- Long-term AERI measurements disclose distinctive DLR trends, demonstrating the advantages of the spectral data for climate monitoring.
- The changes in clear/cloudy sky fractions offset DLR changes caused by warming and increases in greenhouse gases.
- The radiance trend uncertainty mainly results from the natural variability, which emphasizes the need to continue the measurements.

Abstract

Downwelling longwave radiation (DLR) is an important part of the surface energy budget. Spectral trends in the DLR provide insight into the radiative drivers of climate change. In this research, we process and analyze a 23-year downwelling longwave radiance record measured by the Atmospheric Emitted Radiance Interferometers (AERI) at the Southern Great Plains (SGP) site of the Atmospheric Radiation Program. Two AERIs were deployed at SGP with an overlapping observation period of about 10 years, which allows us to examine the consistency and accuracy of the measurements and to characterize discrepancies between them due to undetected instrumentation errors. Using the 23-year record, we analyze the all-sky radiance trends in DLR, which reflects the associated surface warming trend at SGP during this same period and also the complex changes in meteorological conditions. For instance, the observed radiance in the CO_2 absorption band follows closely the near-surface air temperature variations. The changes in the sky fraction of clear-sky and thick cloudy-sky scenes offset the radiance changes in the window band. Our analysis shows that the radiance trend uncertainty in the DLR record to date mainly results from the climate internal variability rather than the measurement error, which highlights the importance of continuing the DLR spectral measurements to unambiguously detect and attribute climate change.

1 Introduction

Longwave radiation is a key component of the atmospheric energy budget that drives climate change. At the top of the atmosphere (TOA), the outgoing longwave radiation (OLR), as well as its spectrally resolved radiance, is monitored by satellites with global coverage and long-term records (e.g., Liebmann & Smith, 1996; Stephens et al., 2012). This allows us to study the changes in OLR and to test climate models (e.g., Harries et al., 2001; Huang & Ramaswamy, 2009; Huang, Ramaswamy, Huang, et al., 2007; Huang, Ramaswamy, & Soden, 2007; Wielicki et al., 2002). Despite the continuous spatiotemporal coverage of OLR spectra, the compensating effects of greenhouse gas opacity and temperature warming make it difficult to detect climate change (Huang & Ramaswamy, 2009).

Downwelling longwave radiation (DLR) emitted by the atmosphere is one key component in the surface energy budget (Stephens et al., 2012; Trenberth et al., 2009). Compared to the radiation budget at the TOA, the surface radiation budget is more uncertain and DLR is a main contributor to the uncertainty (Trenberth et al., 2009; Wild et al., 2012). This is largely due to the lack of global and long-term observations of DLR. DLR observations, especially spectrally resolved radiance, have been limited to specific locations. Despite the limited records, it has been demonstrated that DLR measurements are useful for understanding the surface energy balance and testing the climate models. For example, Lubin (1994) explained the super greenhouse effect using the observed DLR spectra over equatorial oceans; Feldman et al. (2015) used the DLR spectra to measure CO_2 radiative forcing at the Southern Great Plains (SGP) and the North Slope Alaska sites; Shupe and Intrieri (2004), Kapsch et al. (2016), Huang et al. (2019), Sokolowsky et al. (2020) and a number of others diagnosed the DLR variability in relation to sea ice, clouds and other climate changes in polar regions.

Climate change is driven by changes in energy balance. This leads us to an overarching question regarding the surface energy balance: can climate change be detected and understood by monitoring the DLR spectrum? One advantage of the DLR, compared to the OLR, is that the compensating effects mentioned earlier vanishes. In the DLR, the greenhouse gas opacity and temperature warming effects reinforce each other to increase DLR. This makes DLR a potentially advantageous means for monitoring climate change

(Huang, 2013). The signals from different meteorological variables such as temperature, greenhouse gases and clouds imprint different spectral signatures. This allows for a spectral fingerprinting of their changes (Huang et al., 2010). At the SGP site, the fifth generation European Centre for Medium-Range Weather Forecasts atmospheric reanalysis dataset, ERA5 (Hersbach et al., 2020), shows that there has been a significant warming in surface air temperature with a magnitude of ~0.045 K/year between 1996 and 2018 (Figure 1). Can this warming be detected from the DLR spectral records?

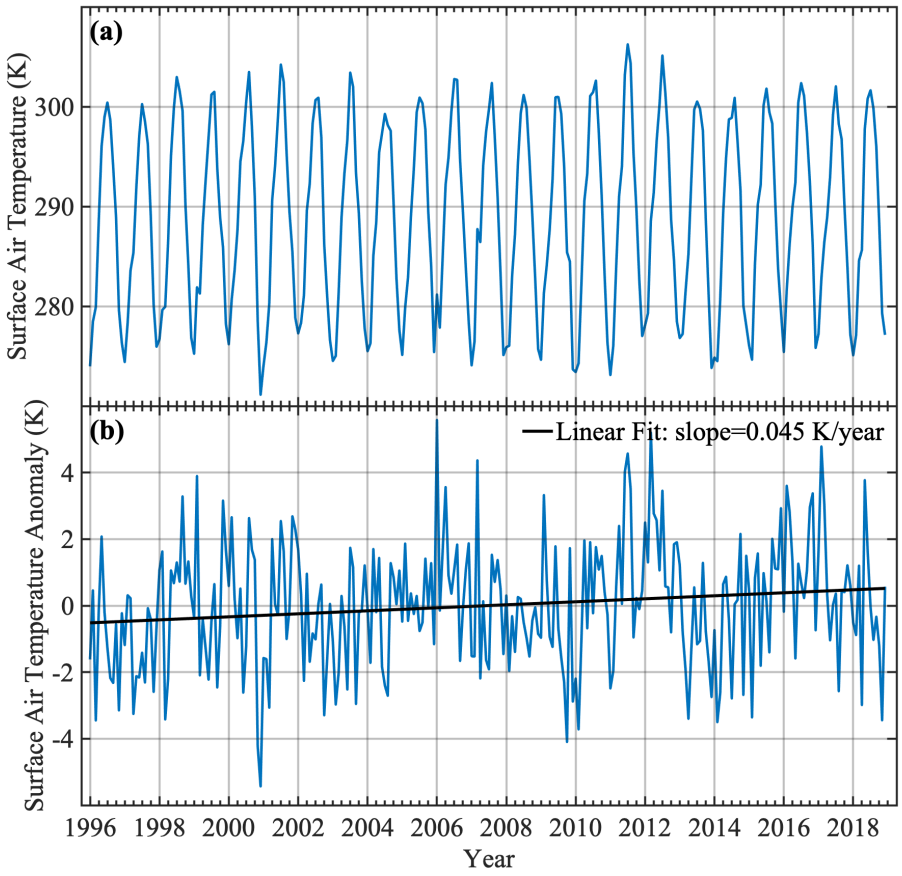

Figure 1. Warming trend at SGP. Shown here is the ERA5 monthly mean 2-meter air temperature time series at the SGP site (average of nine 0.25°x0.25° resolution grid boxes centered at: 97.5° W and 36.5° N) between 1996 and 2018. The anomaly is defined with respect to multi-year monthly mean of each calendar month.

We have two primary objectives in this paper. First, we are interested in constructing a long-term monthly DLR spectral record based on the 23 years of measurements by the Atmospheric Emitted Radiance Interferometers (AERIs) installed at the SGP site of the Atmospheric Radiation Measurement (ARM) program of the U.S. Department of Energy. Two AERI instruments have been deployed at this site and have rendered 10 years of overlapping observations but with different sampling strategies (e.g., 3 min sky average every 8 minutes vs multiple 20-s sky average observations every 4 minutes). We will examine the accuracy and consistency of the measurements and validate them against synthetic spectra simulated from collocated atmospheric measurements using a benchmark radiation model. Second, we will show the analysis of the long-term DLR spectral trends measured by the two AERIs for the period of 1996-2018. We are interested in whether the radiance trends are in concert with the warming temperature trend (Figure 1). This work will also verify the trends documented by Gero and Turner (2011) using the early years of the DLR record and analyze the contributions from different sky conditions.

2 Data and Methods

2.1 AERI data processing

The AERI is a Fourier transform spectrometer that measures the DLR radiance emitted from the atmosphere with good accuracy at high temporal and spectral resolution (Knuteson et al., 2004a, 2004b). The measurements cover the spectral range between 520 and 3020 cm^{-1} with a resolution of 0.5 cm^{-1}. Two high-emissivity blackbodies, a hot blackbody with a fixed temperature at around 60 degrees Celsius and another blackbody at ambient temperature (Knuteson et al., 2004a), are used for radiometric calibration based on the method of Revercomb et al. (1988). The long-term annual mean DLR spectra and the standard deviation of DLR spectra for different sky types (classification method explained later) at SGP site are shown in Figure 2. The main difference in DLR between different sky types is primarily in the window portion of the spectrum (between 800 – 1200 cm^{-1}) shown in Figure 2a. The standard deviation of thick cloudy-sky DLR is found to be the smallest among all the different sky types in the window band (Figure 2b), which indicates small variability of the radiating temperature of the thick clouds. We focus on the mid-infrared spectral range from 520 to 1800 cm^{-1} in this paper.

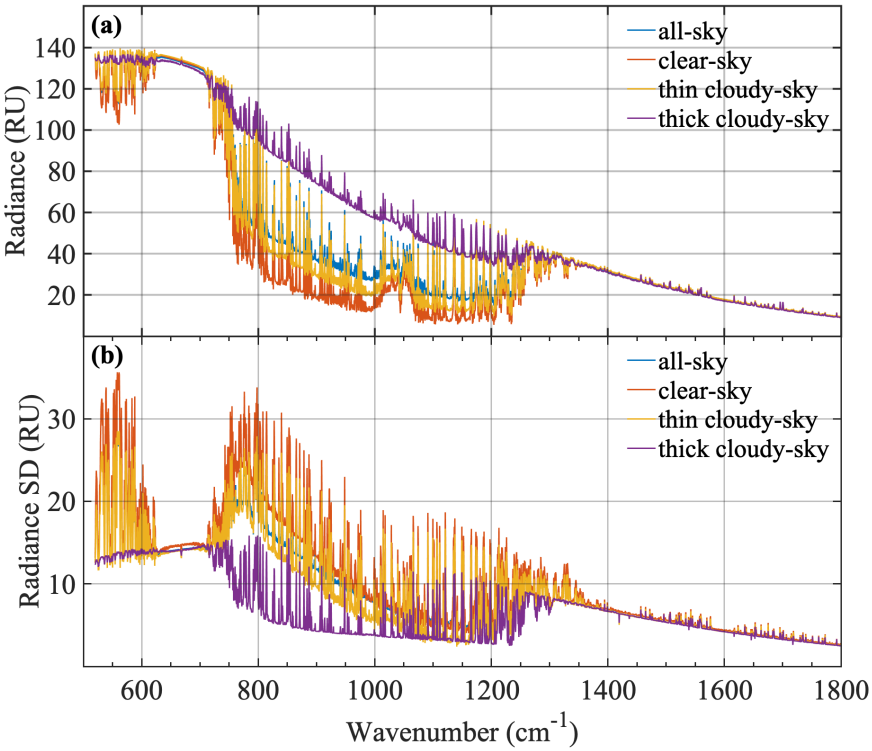

Figure 2. (a) Annual mean AERI spectra for different sky types at SGP. (b) Standard deviation of monthly mean AERI spectra for different sky types at SGP. (RU: Radiance Units; 1 RU = 1 $mW/(m^2\ sr\ cm^{-1})$)

The two AERIs deployed at SGP have different observational periods and different sampling frequencies. AERI-01 operated from July 1995 to March 2014, while AERI-C1 has operated from February 2004 to present. C1 is the current name of the Central Facility location of SGP site which is used to be called E14, e.g. in Gero and Turner (2011). The two AERIs were deployed virtually side-by-side (within 5 meters of each other). Given their field of view (FOV) of 1.3 degrees, both instruments view essentially the same portion of the sky.

The overlapping observations make it possible to test the accuracy and consistency of the measurements. However, the two instruments differ with respect to their sampling frequency. AERI-01 measures one DLR spectrum approximately every 8 minutes; its measurement cycle includes a 200-second sky-dwell period (Knuteson et al., 2004b) and the rest of the cycle is used for viewing the blackbodies for calibration. AERI-C1 uses a rapid mode with a ~20-second sampling cycles (Turner et al., 2006). Such differences in the measurements necessitate appropriate procedures to homogenize the data from the two AERIs for inter-comparisons and trend analyses.

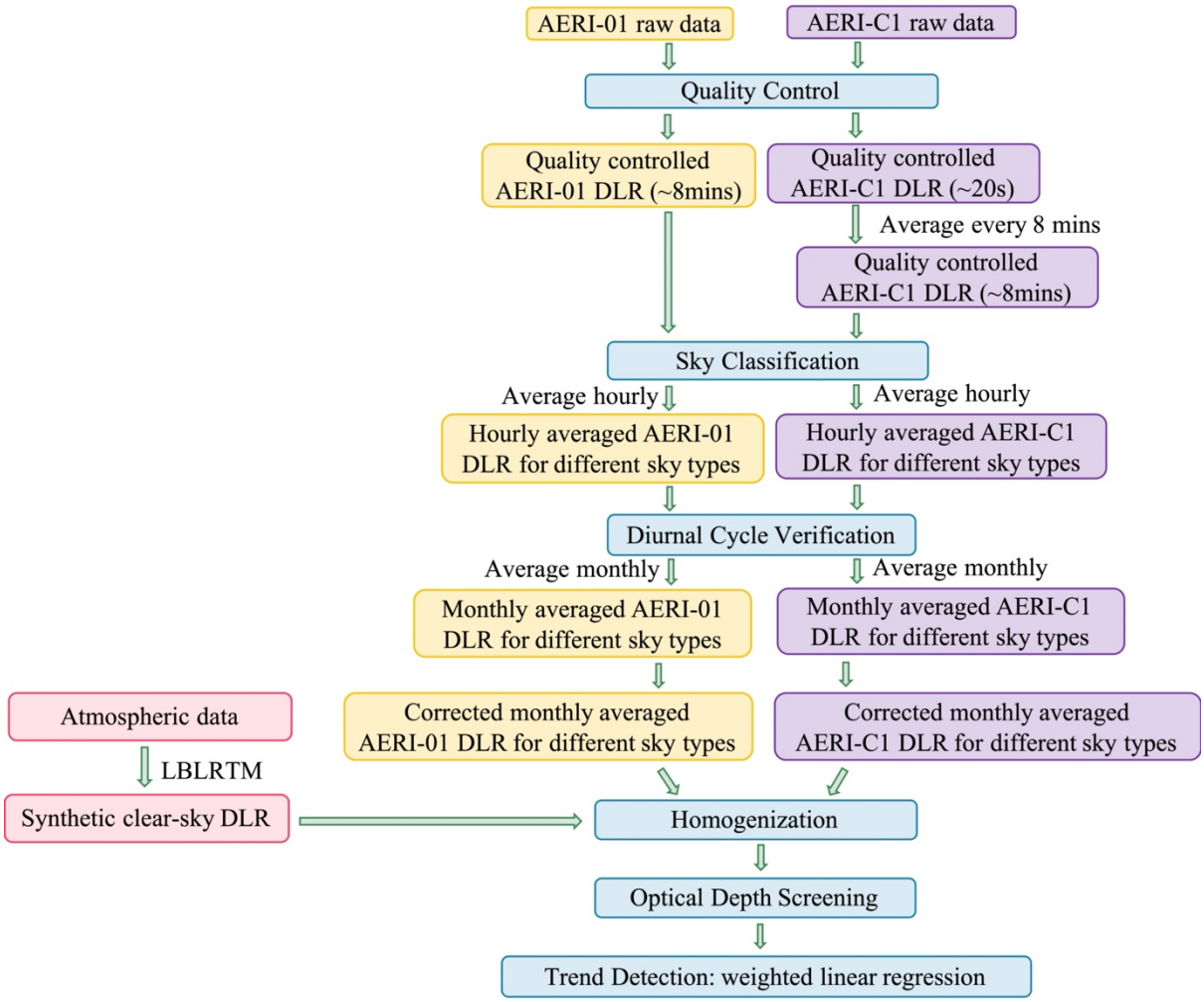

Figure 3. Data processing flowchart. Yellow and purple squares represent AERI-01 and AERI-C1 DLR data respectively. Blue squares represent important data processing steps. Pink squares represent radiative transfer model simulations. (see texts for the details)

Figure 3 shows the flowchart of AERI data processing adopted in this paper. First, rigorous quality control is performed on the data to retain reliable observations. During the long history of observations at the SGP site, many factors have caused errors including: the contamination of the scene mirror, malfunction of the interferometer, the failure of the detector temperature sensor, and so on. We first discard all the erroneous data based on the AERI quality control reports from the ARM program (https://adc.arm.gov/discovery/#/results/instrument_class_code::aeri). In addition, similar to the quality control method described in Turner and Gero (2011), the hatch status and the sky view radiance variability are also implemented.

138 After the *Quality Control* step, we average the AERI-C1 spectra over 8-min intervals,
139 to be consistent with the AERI-01 sampling period. Then, in the *Sky Classification* step, we
140 apply a machine learning algorithm (detailed below) to classify the sky types (clear, thin and
141 thick clouds) based on the 8-min mean radiance spectra. Next, we take hourly averages of the
142 radiance data and verify proper diurnal sampling in each month to ensure no missing data for
143 any 24-hour period. Then the monthly mean spectra are obtained by averaging the 24-hourly
144 spectra of each day during the given month. Monthly means are discarded when the count of
145 hourly spectra is below 400 (~55%).

146 Some channels in the center of CO_2 absorption band (around 667 cm^{-1}) and water
147 vapor absorption band (1300 – 1800 cm^{-1}) in which the near-surface atmosphere is so opaque
148 that the channels are essentially uncalibrated are discarded based on the criterion that the
149 gaseous optical depth for a 1-meter layer of atmosphere at the surface is above 0.5 in the
150 *Optical Depth Screening* step. Finally, the monthly anomaly spectra are obtained by
151 subtracting the long-term monthly spectra of each calendar month (which effectively removes
152 the seasonal cycle). The results are illustrated in Figure 4. The long-term trends in the DLR
153 spectra are analyzed based on the monthly anomaly spectra with the help of synthetic clear-
154 sky DLR to differentiate the measurements of the two AERIs during the overlapping period
155 using the method detailed in Appendix A.
156

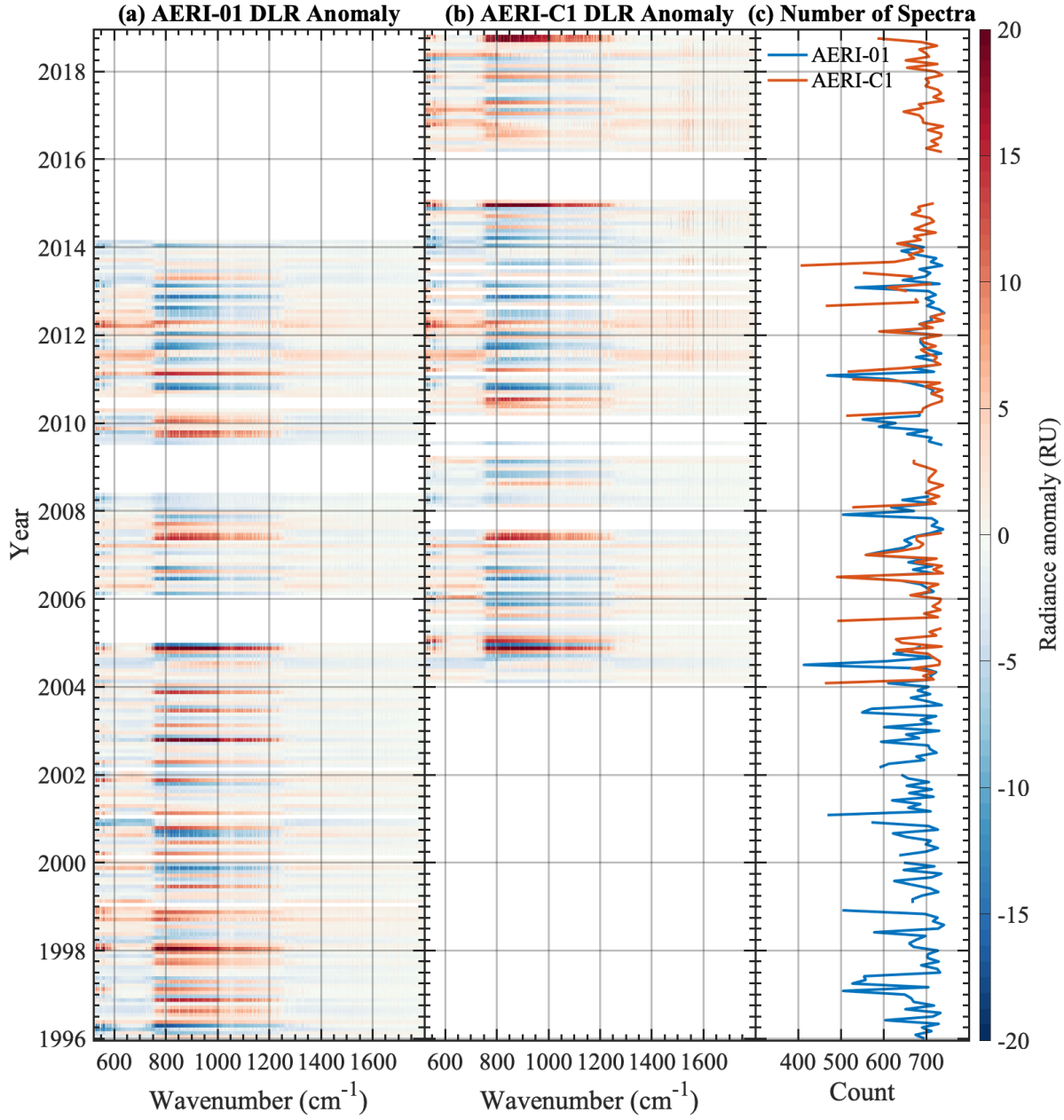

Figure 4. Monthly anomaly of AERI-observed DLR spectra and hourly spectra count in each month.

In most months, the number of hourly mean spectra is larger than 700 (Figure 4c), which means the instruments operated for >95% of the time. The strongest monthly DLR anomalies are seen in the window band (800 – 1200 cm^{-1}). The pattern of the DLR radiance anomalies in the overlapping observational period is very similar between AERI-01 and AERI-C1.

2.2 Sky classification

Clouds strongly influence the DLR flux and spectra, especially in the atmospheric window (800 – 1200 cm^{-1}). In order to identify the causes of the DLR trends, we separate the clear-sky spectra from the cloudy ones and to examine their trends separately.

A sky classification model is developed using a machine learning method, the k-nearest neighbor (k-NN) algorithm(Cunningham & Delany, 2020). The 8-min AERI-01 and AERI-C1 data between March 1, 2011 to July 31, 2012 are used to train the k-NN model. We use the same inputs and truth data from Raman Lidar as in Turner and Gero (2011). The k-NN classification achieves an accuracy of 94.8%. This algorithm determines the sky to be *clear* or *cloudy*, while the cloudy sky is then further classified to be *thin-cloud* when the 70-minute averaged 985 cm^{-1} brightness temperature is lower than 250K; otherwise, it is classified to be *thick-cloud*. We also tried a classical backpropagation gradient-descent classification algorithm as used by Turner and Gero (2011), which achieves an accuracy of 90%. The resulting trends are not sensitive to the classification method chosen. The results presented below are based on the k-NN algorithm.

Based on the classification of the *thin-cloud* and *thick-cloud*, the *thick-cloud* emitting temperature range is smaller than that for *thin-cloud* and *clear-sky*, primarily because *thick-clouds* are opaque clouds relatively close to the surface while *thin-cloud* may be either partially cloudy scenes or clouds higher in the troposphere. This is why the *thick-cloud* classification has the smallest standard deviation of DLR among all three different sky conditions.

2.3 Homogenization

During the overlapping observational period, discrepancies larger than the documented AERI absolute calibration uncertainty (Knuteson et al., 2004a) were noticed between the monthly mean spectra observed by AERI-01 and AERI-C1. Large radiance discrepancies occur especially in the window band and are found to mainly come from clear-sky scenes (see Figure B1 and discussions in Appendix B). This suggests that the discrepancies likely result from calibration(Rowe, Neshyba, Cox, et al., 2011; Rowe, Neshyba, & Walden, 2011) and other undetected errors. In order to avoid discarding meaningful data in the trend analysis, we simulate the clear-sky DLR spectra using a radiation model from the collocated atmospheric measurements and use the synthetic spectra as a reference to assign proper weights in combining the data of AERI-01 and AERI-C1, based on the findings of previous radiance closure studies (e.g., Turner et al., 2004) that demonstrated high accuracy in such synthetic spectra.

The radiation model used here is the Line-by-Line Radiative Transfer Model (LBLRTM v12.9) (Clough et al., 2005). To synthesize the clear sky DLR spectra at SGP, we use the temperature and water vapor profiles from the ARM Balloon-Borne Sounding System (https://www.arm.gov/capabilities/instruments/sonde). The water vapor mixing ratio profiles derived from radiosonde are scaled with a height-independent factor to match the precipitable water vapor determined by the microwave radiometer at SGP site. This approach has been used to compensate the dry-bias issue found in the radiosonde water vapor data (Holdridge, 2020; Revercomb et al., 2003; Turner et al., 2003; Wang et al., 2002). CO_2 and CH_4 concentration profiles are obtained from the CarbonTracker website (http://carbontracker.noaa.gov, Jacobson et al., 2020; Peters et al., 2007). O_3 concentration profiles are adjusted from NASA's Modern-Era Retrospective analysis for Research and Applications, Version 2 (MERRA-2, Gelaro et al., 2017) ozone product to get a better radiative closure with AERI observed DLR (see more details in Appendix B). We use a 200-level input profile for the LBLRTM simulations. The first and second levels are at 0m and 10m above ground level respectively. The depth of each subsequent layer is increased by 2% relative to the previous one.

As radiosonde observations of near-surface layers are essential to the DLR spectra, the AERI data are selected to match the radiosonde launch time. We keep the spectra whose observation time is within 10 minutes of the radiosonde launch time. For each month, about 70 clear sky downwelling longwave spectra are simulated on average. The absolute radiance biases (R_{bias}) are determined as the monthly mean radiance differences between the synthetic and observed DLR spectra.

During the overlapping observational period, the monthly mean DLR is combined from AERI-01 and AERI-C1 observed DLR according to Equation (1) and Equation (2) by assigning a ratio r, which represents the proximity of the AERIs observed DLR spectra to the synthetic DLR spectra. In Equation (2), $R_{AERI-01}$ and $R_{AERI-C1}$ represent the observed AERI-01 and AERI-C1 monthly mean DLR respectively.

$$r = \frac{R_{bias(AERI-01\,-LBLRTM)}}{R_{bias(AERI-C1\,-LBLRTM)}} \tag{1}$$

$$R = R_{AERI-01} \times \frac{1}{1+r} + R_{AERI-C1} \times \frac{r}{1+r} \tag{2}$$

2.4 Trend detection

A weighted linear regression method is applied to detecting the DLR radiance trends. We develop our weighted linear regression model based on the regression model developed by Tiao et al. (1990) and Weatherhead et al. (1998).

This model determines the radiance trend, $\hat{\omega}$, in each AERI channel as:

$$\hat{\omega} = \frac{\sum_{t=1}^{T} W_t\left(t-\bar{t}\right)y_t^{\star}}{\frac{1-\phi}{12}\sum_{t=1}^{T} W_t(t-\bar{t})^2} \tag{3}$$

In Equation (3), T represents the total number of months. ϕ is the autocorrelation in the noise of the time series considering a first-order autoregressive (AR1) process, and $y_t^{\star}$ represents the transformed radiance anomalies (see Figure A1) after removing the effect of the AR1 process (see details in Appendix A). W_t represents the weights which is determined as the intra-month variability of the all-sky observed DLR, shown in Equation (4):

$$W_t = \frac{N_t}{{\sigma_t}^2} \tag{4}$$

where N_t and ${\sigma_t}^2$ represent the number and variance of hourly observations in each month. Large variability of DLR radiance results in smaller weights. We use the same weights for all sky types.

Along with the magnitude of the trend it is also important to determine the associated uncertainty, $\sigma_{\hat{\omega}}$, which is shown in Equation (5). Here, we mainly account for two sources of uncertainty. First, there is the uncertainty arising from the internal climate variability. This is measured by the term in Equation (5) associated with σ_N and ϕ. Second, there is the uncertainty arising from instrumentation errors measured by the term in Equation (5) associated with σ_e. We assume that two sources of uncertainty are independent of each other. The derivation of Equation (5) is given in Appendix A.

$$\sigma_{\hat{\omega}} = \frac{12\sqrt{\sum_{t=1}^{T} {W_t}^2(t-\bar{t})^2}}{\sum_{t=1}^{T} W_t(t-\bar{t})^2}\sqrt{{\sigma_N}^2\frac{1+\phi}{1-\phi}+{\sigma_e}^2} \tag{5}$$

The derived $\sigma_{\hat{\omega}}$ in Equation (5) is referred to as the standard error of the trend magnitude. It is used to test whether the trends deviate significantly from 0 at the 95% significance level. A trend is considered to be significant at the 95% significance level if the trend magnitude is roughly larger than $2\sigma_{\hat{\omega}}$. In following figures, the uncertainty envelope corresponds to the 95% confidence interval.

3 Results

3.1 All-sky radiance trends

The homogenized downwelling longwave radiance records have been constructed, based on monthly averaged AERI-01 data from 1996 to 2013 and AERI-C1 data from 2004 to 2018. In total, we have 23 years of DLR data at SGP for analysis.

It can be inferred from the monthly anomalies shown in Figure 4 that the DLR radiance trends depend on the analysis period as the anomalies do not show monotonic changes over this 23-year period. It is noticeable that AERI-01 data (Figure 4a) show decreasing trends in window-band (800-1200 cm^{-1}) DLR, which is consistent with the negative trends detected in Gero and Turner (2011). Including AERI-C1 data (Figure 4b) affords a longer DLR spectral record; the latest few years are especially characterized by warm anomalies.

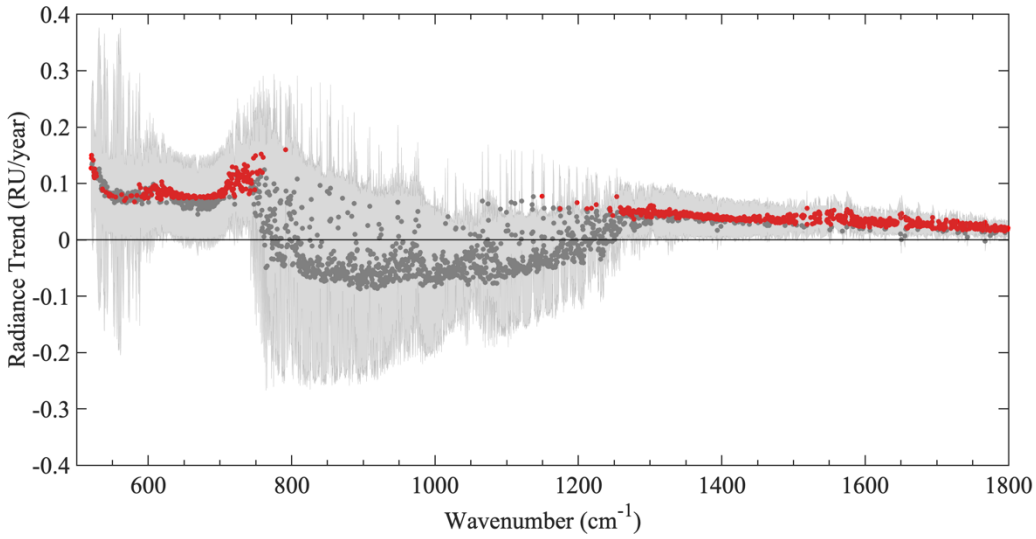

Figure 5. The all-sky radiance trends. Each dot represents the trend at a different AERI channel and the trends in reds pass the 95% significance test while the grey ones do not. The shading in the figure is the 95% confidence interval.

The long-term all-sky radiance trends over the period of 1996-2018 are shown in Figure 5. The all-sky DLR trends have different features in different spectral bands. In the CO_2 absorption band centered around 667 cm^{-1}, the trends are generally positive (increasing) and are statistically significant in the wings but not at the center. In the window band (800-1200 cm^{-1}), there are no statistically significant trends. In the water vapor absorption band (1300-1800 cm^{-1}), similar to the CO_2 absorption band, the radiance trends are generally positive and statically significant.

DLR radiance in different AERI channels are controlled by different meteorological variables. To illustrate this point, Figure 6a shows the correlation coefficients between the deseasonalized and detrended monthly anomalies in the radiance (brightness temperature)

spectra from the two AERIs and surface air temperature from ERA5. Note that AERI-01 and AERI-C1 have different observational periods, which can cause the correlation coefficients difference between AERI-01 and AERI-C1 especially in the window band. In the center of the CO_2 absorption band (667 cm^{-1}) and channels corresponding to strong H_2O absorption lines, the correlation coefficient is close to one, indicating that the variance in the radiance in these channels is primarily controlled by the surface air temperature. This is because the atmospheric absorption is strongly saturated in these channels and thus they are less sensitive to variations in the concentrations of the gases themselves. In comparison, at the wings of the CO_2 band and the weaker H_2O absorption lines, the atmospheric absorption is not saturated so that variability in DLR radiance is subject to the variation in the temperature and gas concentration, meaning that the trends both in temperature and gas concentrations drive the radiance to increase, which explains the stronger and statistically more significant trend signals in these channels, as seen in Figure 5.

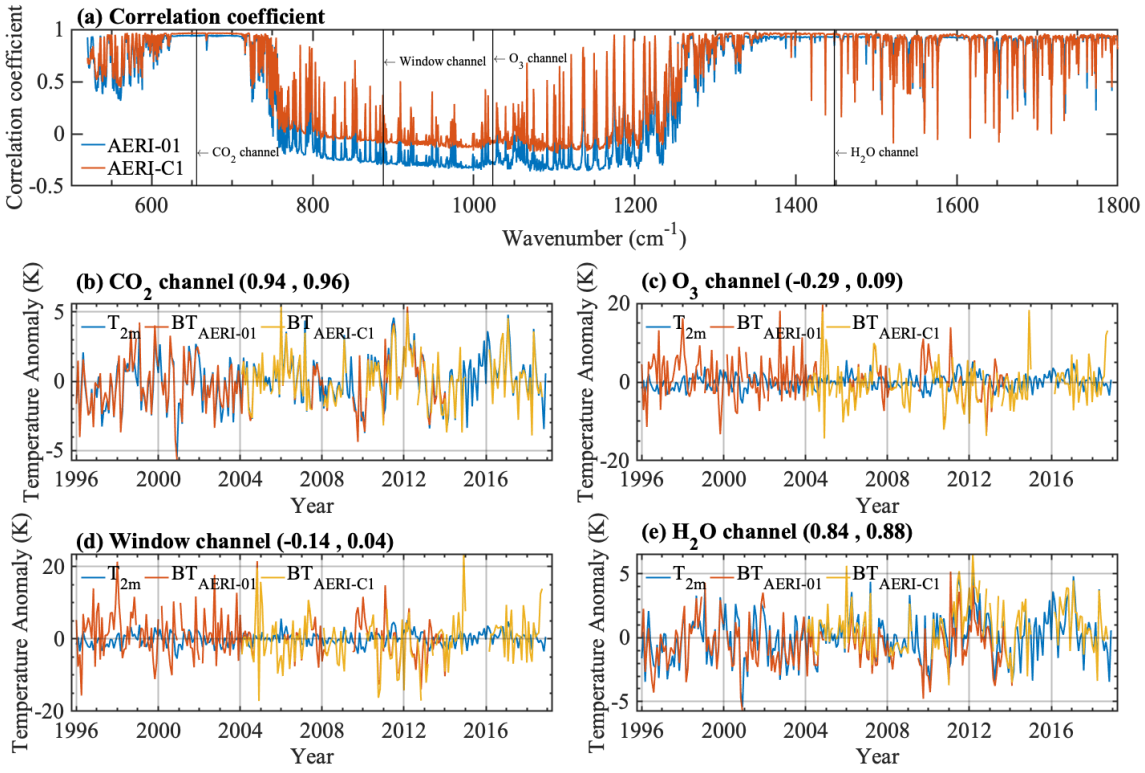

Figure 6. (a)The correlation coefficient between the AERI observed brightness temperature spectra and near surface air temperature from ERA5. (b-e) The time series of the deseasonalized brightness temperature and near surface air temperature in four AERI channels. In each title, the values in the brackets are the correlation coefficients between near surface air temperature from ERA5 and observed brightness temperature by AERI-01 and AERI-C1 respectively.

In Figure 6, the time series of the brightness temperature in four selected AERI channels: a CO_2 channel at 655.72 cm^{-1}, a window channel at 887.63 cm^{-1}, a O_3 channel at 1023.60 cm^{-1}, and a H_2O channel at 1447.89 cm^{-1} (Figure 6b to 6e) are displayed. There is good consistency between the AERI-01 and AERI-C1 observed brightness temperature in all four channels. The all-sky brightness temperature at the CO_2 channel follows closely with the surface air temperature from ERA5 (Figure 6b). The near-surface warming of 0.045 K/year (Figure 1) is equivalent to 0.071 RU/year at this channel, which is close to the observed all-sky radiance trend of ~0.072 RU/year (averaged trend between nearby 5 channels). In the H_2O channel, the brightness temperature measured by the AERIs also follows the near

surface air temperature (Figure 6e) but not as close as the CO_2 channel (Figure 6b). In contrast, the brightness temperature anomalies in the window and O_3 channels have larger fluctuations than that at the CO_2 and H_2O channels and are evidently decoupled from the near surface air temperature (Figure 6c and 6d).

That the radiance trend is reinforced by the warming and opacity effects in the weak absorption channels leads to benefits of using these AERI measurements in climate change detection. Assuming the trend magnitude and uncertainty determined from the 23-year records hold unchanged into future, the years to detect a significant trend, $n^{\star}$, at 90% significance level is:

$$n^{\star} \approx \frac{3.3\sigma_{\hat{\omega}}}{|\hat{\omega}|} \times 23\ years \tag{6}$$

where $\hat{\omega}$ is the 23-year trend determined by Equation (3) and $\sigma_{\hat{\omega}}$ is the trend uncertainty determined by Equation (5). Based on this equation, approximately 30 years are needed to detect a significant trend in the 2-meter air temperature from the ERA5 data shown in Figure 1. In comparison, Figure 7 shows earlier detectability of the radiance trends in weak absorption channels, such as in the wings of the CO_2 band and in the weak absorption channels in the H_2O vibration-rotational band. We can conclude that it is advantageous to monitor the DLR radiance in these channels for climate change detection.

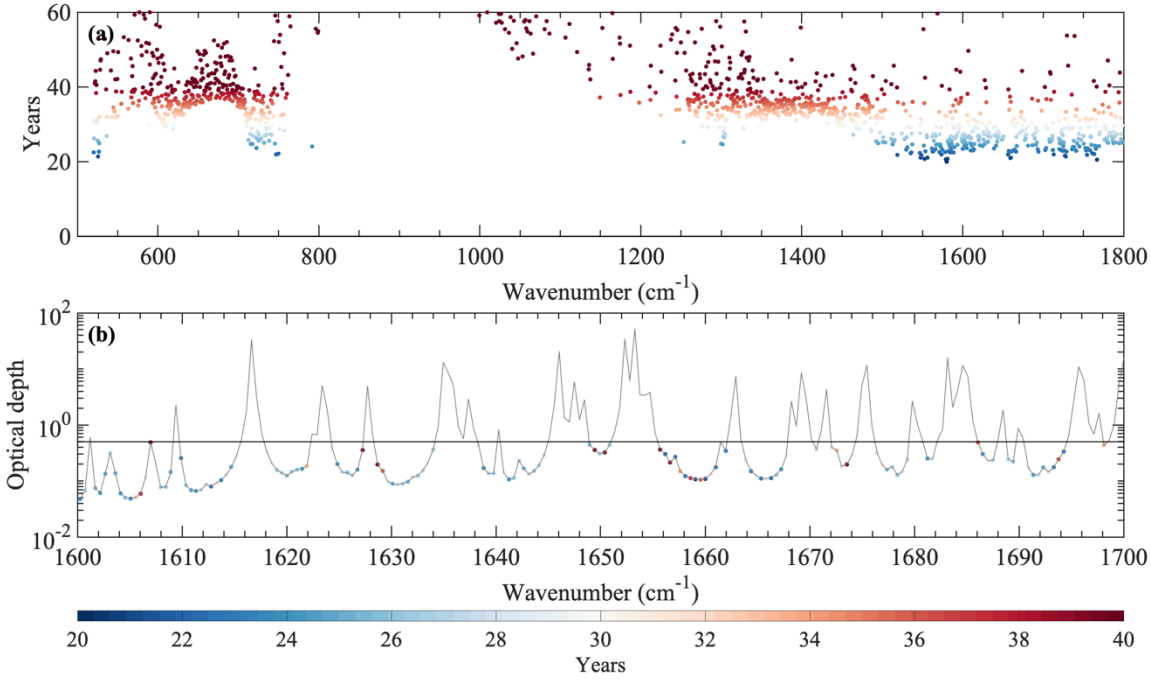

Figure 7. Trend detectability. (a) Time to detect (T2D) radiance trends at 90% significance level in different AERI channels; in comparison, the T2D for the 2-meter temperature from the ERA5 reanalysis is about 30 years. (b) The T2D (color-coded), in relation to atmospheric absorption strength, measured by the optical depth of a 1-meter-thick atmospheric layer near the surface. The horizontal line marks optical depth of 0.5.

Trend detection in the radiance record is determined by comparing the trend signal to the uncertainties arising from different causes. Here, based on Equation (5), we account for uncertainties arising from climate internal variability (σ_N) and also instrumentation error (σ_e) (Figure 5). The overall uncertainty is notably large in the window band for the all-sky condition (Figure 5) or for different sky conditions (Figure 9), which impedes the detection of

any significant radiance trends in this especially variable spectral band. The analysis of the respective parameters in Appendix A (see Figure A2) indicates the climate internal variability dominates the instrumentation error when shaping the overall uncertainty envelope in Figure 5. It is found that the influence of the autoregressive process also does not strongly influence the trend uncertainty, as evident by the small value of ϕ, especially in the window band. We conclude that the trend uncertainty mainly arises from the internal climate variability.

3.2 Trends in different cloud conditions

The results presented in the previous subsection demonstrate that the radiance trends in the window band are different from the greenhouse gas absorption bands; the window band also is prone to high levels of uncertainty due to the marked variability of the signal that ranges from small values in clear sky conditions to large values when opaque low-altitude clouds are overhead. Given the fact that clouds are a significant factor that influences this band (see Figure 2), we analyze the radiance trends under different cloud conditions in this subsection.

The fraction of time that each sky conditions occur in one month (referred as 'sky fractions') based on the hourly spectra are shown in Figure 8. First, there is a good agreement between AERI-01 and AERI-C1 in the sky fraction monthly time series, with correlation coefficients of 0.94, 0.89, and 0.94 for clear-sky, thin cloudy-sky, and thick cloudy-sky, respectively. The clear-sky fraction between June 1996 and May 2010 from our classification is around 42% which is comparable to what was found by Turner and Gero (2011).

The clear-sky fraction increases at a rate of 0.17±0.09 % per year, while the thick cloudy-sky fraction decreases at a rate of -0.18±0.09 % per year. There is no significant trend for thin cloudy-sky fraction. The reason why the sky fraction trends for different sky conditions are different warrant further investigation in future work.

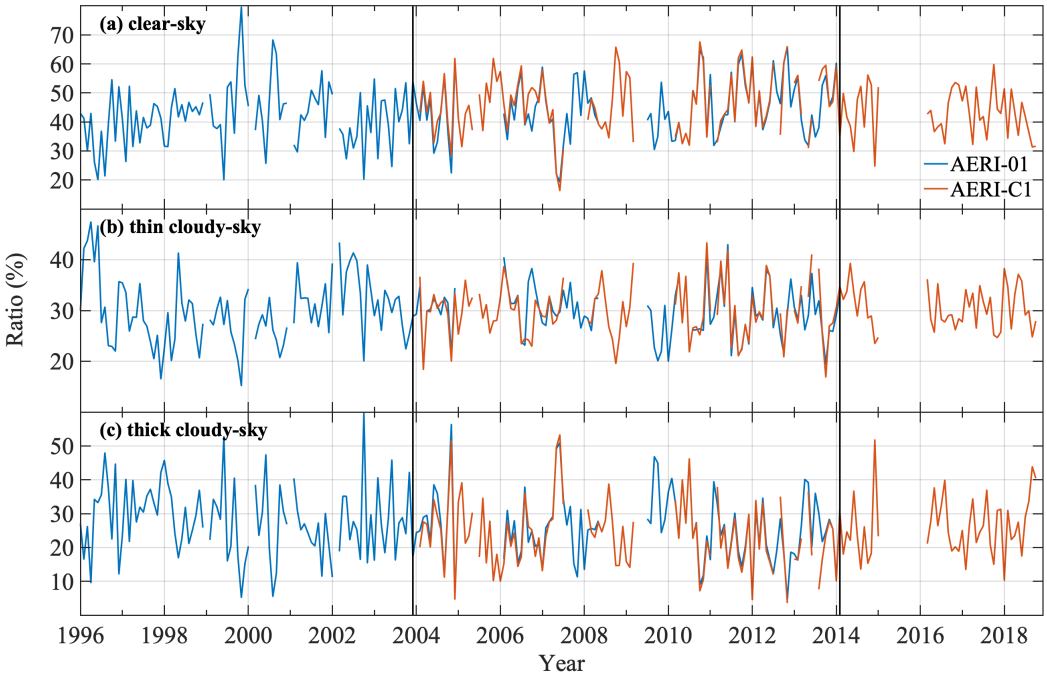

Figure 8. The monthly sky fractions of different sky conditions, categorized based on 8-minute mean spectra at SGP site. The overlapping observational period is between the two vertical thick black lines.

Trends in DLR radiance for different sky types based on the k-NN classifier are shown in Figure 9. In the window band, the clear-sky and thin cloudy-sky trends are positive, while the thick cloudy-sky trends are negative; however, none of those trends is statistically significant from zero. In the spectral regions outside the window band, the trends for different sky types are generally positive and have the same features as the all-sky scene.

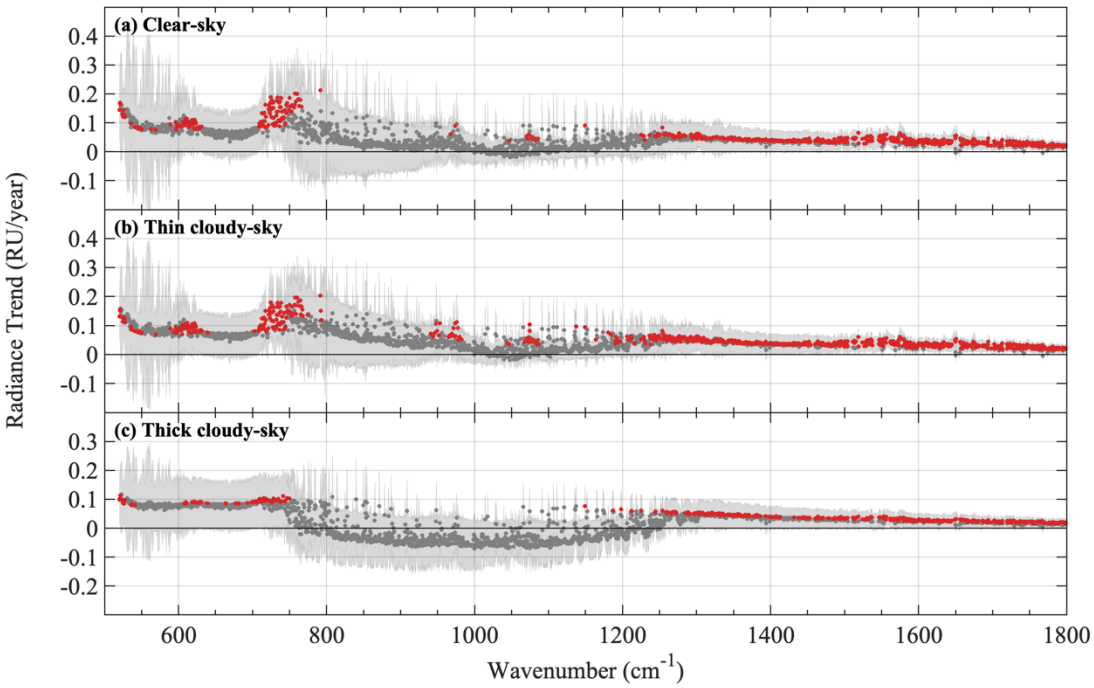

Figure 9. The trends in DLR radiance for different sky types at SGP site. Each dot represents the trend at a different AERI channel and the trends in red pass the 95% significance test while the grey ones do not. The shading in the figure is the 95% confidence interval.

The all-sky DLR trends is caused by changes in both sky fraction and radiance of each sky type. We use equation (7) to separate the contributions from these factors, in which R_{all} represents the all-sky radiance, f_i and R_i represent the sky fraction and mean radiance for different sky types.

$$\frac{dR_{all}}{dt} = \sum \frac{df_i}{dt} R_i + \sum \frac{dR_i}{dt} f_i + residual \quad (7)$$

The results of decomposed trends based on Equation (7) are shown in Figure 10. The small residual term (purple line in Figure 10a), which comes from the nonlinear effects, suggests that the overall all-sky radiance trends can be well explained by Equation (7). In the window band, the overall radiance trends are a result of the compensation between the sky fraction change (orange line in Figure 10a) and the radiance change (yellow line in Figure 10a). While in the CO_2 absorption band (centered at 677 cm^{-1}) and H_2O absorption band (1300 – 1800 cm^{-1}), the overall radiance trends are caused by radiance change which is due almost entirely to the increases in the near-surface temperature because the atmosphere is already too opaque to reflect any gas concentration changes.

The overall radiance trends caused by sky fraction changes (orange line in Figure 10a) are a result of the compensation between changes in the clear-sky (blue line in Figure 10b) and the thick cloudy-sky fraction (yellow line in Figure 10b). In the CO_2 absorption band (centered at 677 cm^{-1}) and H_2O absorption band (1300 – 1800 cm^{-1}), there is a perfect

compensation resulting in almost no trends. In the window band, the negative trends are mainly caused by the thick cloudy-sky fraction change.

In the window band (800 -1200 cm^{-1}), the overall radiance trends caused by radiance change (yellow line in Figure 10a) result from the compensation between positive clear-sky and thin cloudy-sky radiance change trends and negative thick-cloudy sky radiance change trends. While in the CO_2 absorption band (centered at 677 cm^{-1}) and H_2O absorption band (1300 – 1800 cm^{-1}), the radiance changes for the three sky types all contribute similarly to the overall radiance trends caused by radiance change.

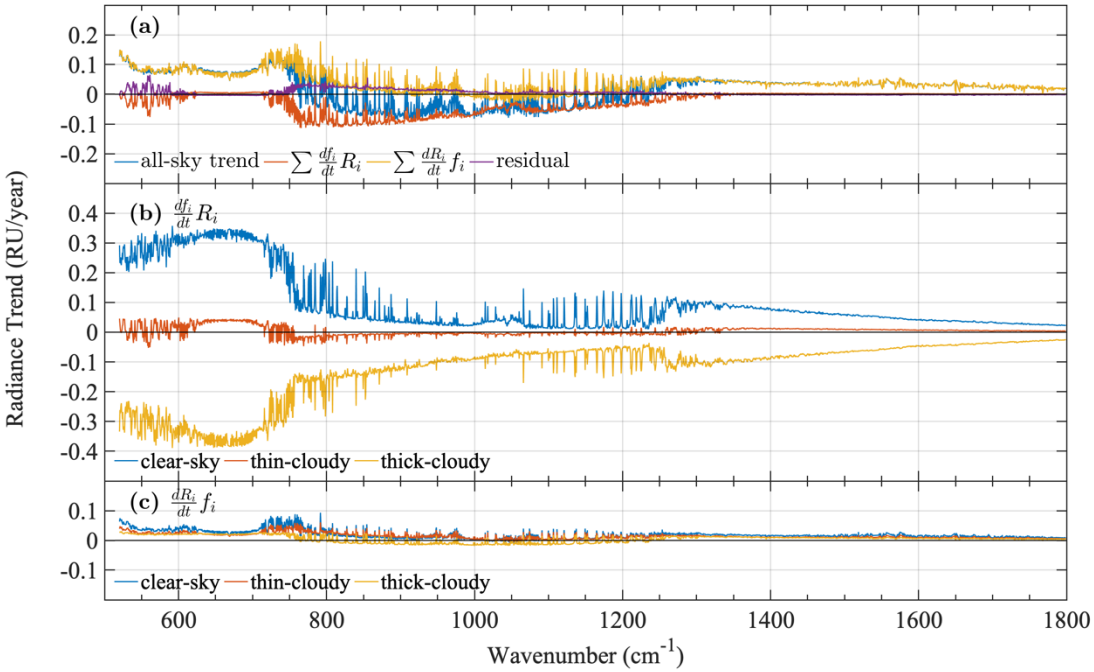

Figure 10. The all-sky DLR trends decomposed to the contributions from the sky fraction and radiance changes of different sky types. (a) The blue line represents the calculated all-sky DLR trends which is the same as that from Figure 5. Orange and yellow lines represent the contribution from sky fraction change and radiance change determined using equation (7) respectively. The purple line is the residual term from Equation (7); (b) The all-sky DLR trends caused by sky fraction change. The blue, orange, and yellow lines represent the contributions from clear-sky, thin cloudy-sky, and thick cloudy-sky fraction changes respectively; (c)The all-sky DLR trends caused by radiance change. The blue, orange, and yellow lines represent the contributions from clear-sky, thin cloudy-sky, and thick cloudy-sky radiance changes respectively.

4 Discussion and Conclusions

In this study, a long-term record of DLR at SGP site have been constructed for analyzing the DLR trends, based on a weighted linear regression method which considers both natural climate variability and measurement error. Compared to previous studies, our analysis is based on a longer DLR record combined from the two AERIs at the SGP site and makes use of synthetic DLR data in validating and differentiating the AERI measurements over their overlapping observational period. In addition, we quantitatively decompose the overall radiance trends due to the contributions from sky fraction change and radiance change.

The trends in DLR in different spectral ranges have different features. The trends are generally positive in the CO_2 and H_2O absorption bands, while no statistically significant trends are detected in the window band (Figure 5). We find that in the centers of the CO_2 and H_2O absorption bands, the radiance are controlled by the near-surface air temperature (Figure 6) because of the strong saturated atmospheric absorption. The sensitivity of DLR to near-surface air temperature indicates the potential of DLR to monitor climate change. In the wings of these absorption bands, both the near surface atmospheric warming and the increase of the abundance of these trace gases contribute to the radiance trends (Feldman et al., 2015), which makes climate trend signal more readily detectable, as hypothesized by Huang (2013). In the window band, the radiance are decoupled from the near surface air temperature (Figure 6) because of the impact of sky-fraction changes of different scenes (clear and cloudy-skies).

We find that the sky fraction change and the radiance change led to compensating effects on the DLR trends. This compensation results in weakly (statistically insignificant) negative radiance trends in the window band (Figure 10). In contrast, the radiance trends are dominated by the radiance change in the CO_2 and H_2O absorption bands, which are similar in all three sky types.

The influences of both climate natural variability and measurement error are considered when determining the uncertainty of the trend magnitude (Equation (5), Figure A2). We find that for all the sky types, the majority of the uncertainty comes from the natural variability. This underlines the necessity of continuous DLR measurements to ascertain the DLR trends, especially in the mid-infrared window (Figure 5).

The two AERIs at the SGP site provide us an excellent opportunity to test the accuracy and consistency of the instruments. The discrepancies between the two AERIs in the overlapping periods may have come from calibration error and other undetected instrumentation errors. In this study, we use synthetic data to differentiate and combine the two AERIs' observations. Further investigation is required to understand the origin of the discrepancies and therefore to assure the measurement accuracy.

This paper has focused on the detection, as opposed to attribution, of the DLR trends. In the clear-sky case, atmospheric temperature and radiative gas concentration changes (primarily in water vapor) are likely the main contributors to the DLR radiance changes. As for the cloudy-sky case, changes in both the atmospheric states and cloud properties may contribute to the DLR radiance changes. Future work is warranted to understand and quantitatively attribute the DLR trends disclosed in this paper to different meteorological variables.

Acknowledgments

This work is supported by grants from the Fonds de Recherché Nature et Technologies of Quebec (PR-283823) and the Canadian Space Agency (19FAMCGB16). LL acknowledges the support of a Milton Leong Graduate Fellowship of McGill University. The original AERI data can be achieved from the ARM data repository (http://www.arm.gov). Our processed monthly mean AERI spectra is available from Mendeley Data (https://data.mendeley.com/datasets/hdwfm3zpd8/1). CarbonTracker CT2019B results provided by NOAA ESRL, Boulder, Colorado, USA from the website at http://carbontracker.noaa.gov. CarbonTracker-CH4 results provided by NOAA ESRL, Boulder, Colorado, USA from the website at http://www.esrl.noaa.gov/gmd/ccgg/carbontracker-ch4/.

Appendix A: Trend Detection

We first summarize the linear trend model and trend estimation from Tiao et al. (1990) and Weatherhead et al. (1998) in A.1 and A.2. We adopt the same notation in their papers. Then we add the measurement error term to the trend detection in A.3 following Tiao et al. (1990).

A.1 Basic linear trend modeling

In order to detect the linear trend, we first construct a simple model that describes the monthly mean radiance Y_t as:

$$Y_t = \mu + S_t + \omega X_t + N_t, t = 1, \cdots, T \quad (A1)$$

where μ is a constant term, S_t represents the seasonal component, ω is the trend magnitude to be determined, $X_t = \frac{t}{12}$ represents time measured in the units of year, N_t represents the unexplained portion of the data, i.e. the noise, and T represents the length of data set in months.

The seasonal component S_t is determined by taking long-term average of each calendar month. This component is subsequently removed from the monthly mean.

$$y_t = Y_t - S_t = \mu + \omega X_t + N_t, t = 1, \cdots, T \quad (A2)$$

The noise N_t is assumed to be autoregressive of the order of 1 (AR1):

$$N_t = \phi N_{t-1} + \epsilon_t \quad (A3)$$

where ϵ_t are the random white noise with zero mean and common variance ${\sigma_\epsilon}^2$, $\epsilon_t \sim W(0, {\sigma_\epsilon}^2)$. The autocorrelations in the noise come from various natural factors. ϕ is determined as the autocorrelation coefficient of the AR1 process after removing from y_t a linear trend component obtained by regressing y_t to time using a simple weighted linear least squares method (i.e., neglecting the AR1). The all-sky ϕ is shown in Figure A2a.

The variance of the noise N_t can also be determined from the detrended y_t time series:

$$\begin{aligned} {\sigma_N}^2 &= Cov(N_t, N_t) = Cov(\phi N_{t-1} + \epsilon_t, \phi N_{t-1} + \epsilon_t) \\ &= \phi^2 Cov(N_{t-1}, N_{t-1}) + Cov(\epsilon_t, \epsilon_t) \\ &= \phi^2 {\sigma_N}^2 + {\sigma_\epsilon}^2 \end{aligned} \quad (A4)$$

Thus,

$${\sigma_N}^2 = \frac{{\sigma_\epsilon}^2}{1 - \phi^2} \quad (A5)$$

A.2 Trend estimation with weights

Given ϕ, to obtain the trend estimation, we consider a transformed model:

$$\begin{aligned} y_t^\star &= y_t - \phi y_{t-1} \\ &= \mu(1-\phi) + \omega(X_t - \phi X_{t-1}) + \epsilon_t \\ &= \mu(1-\phi) + \omega\left[\frac{t - \phi(t-1)}{12}\right] + \epsilon_t \\ &= \mu(1-\phi) + \frac{\omega\phi}{12} + \frac{\omega(1-\phi)t}{12} + \epsilon_t \\ &= \mu^\star + \omega t^\star + \epsilon_t \end{aligned} \quad (A6)$$

where $\mu^\star = \mu(1-\phi) + \frac{\omega\phi}{12}$ and $t^\star = \frac{(1-\phi)t}{12}$. Thus, in the transformed model, there is no more noise term N_t.

The transformed DLR radiance ${y_t}^\star$ is shown in Figure A1.

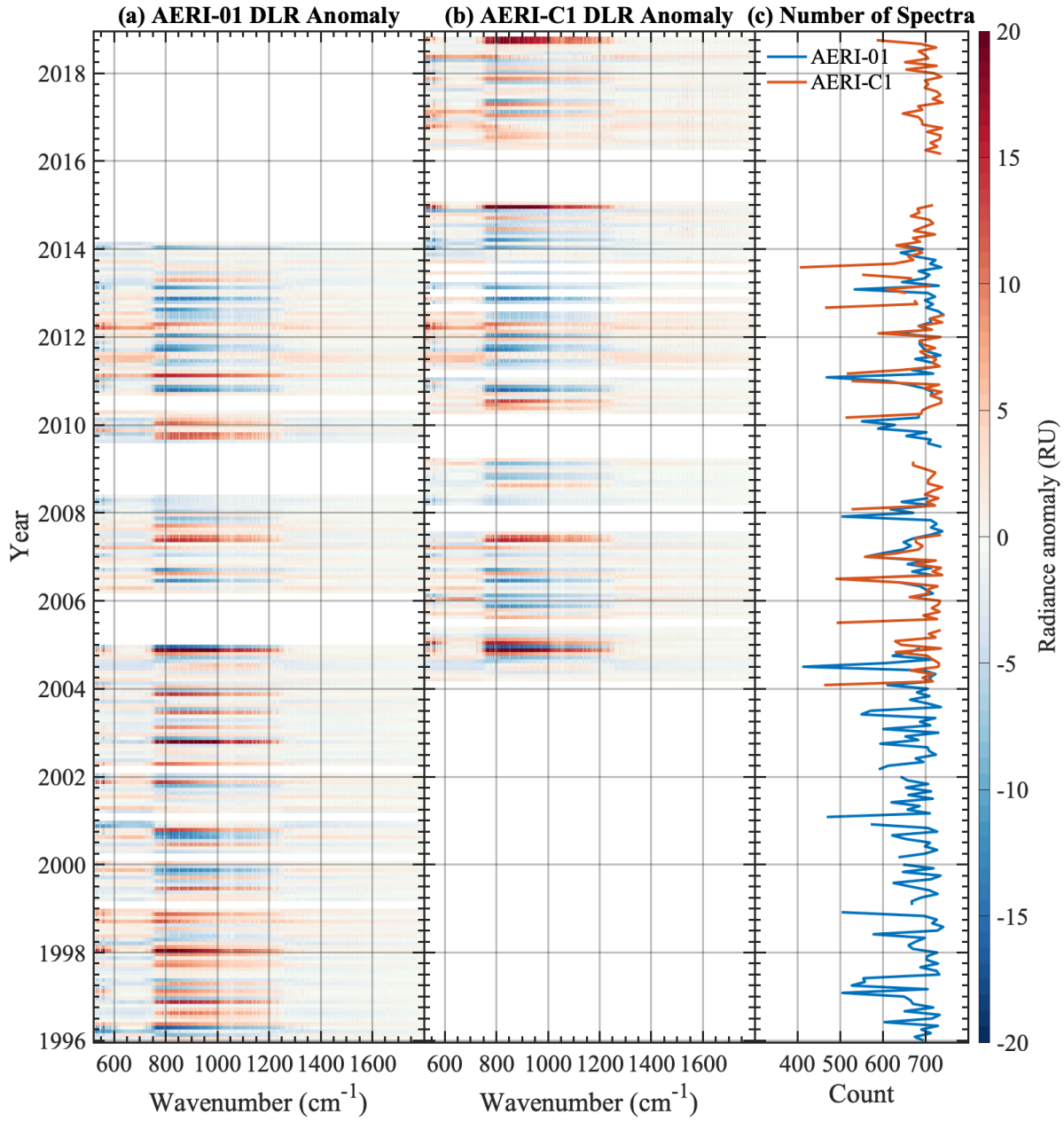

Figure A1. Transformed monthly anomaly of AERI-observed radiance based on Equation (A6).

According to the weighted least square estimation:

$$\widehat{\omega} = \frac{\sum_{t=1}^{T} W_t(t^\star - \overline{t^\star}){y_t}^\star}{\sum_{t=1}^{T} W_t(t^\star - \overline{t^\star})^2} = \frac{\sum_{t=1}^{T} W_t(t-\bar{t}){y_t}^\star}{\frac{1-\phi}{12}\sum_{t=1}^{T} W_t(t-\bar{t})^2} \qquad (A7)$$

where W_t represents the weights determined according to Equation (4), $\overline{y_t^\star} = \frac{\sum_{t=1}^{T} W_t y_t^\star}{\sum_{t=1}^{T} W_t}$, $\bar{t}^\star = \frac{\sum_{t=1}^{T} W_t t^\star}{\sum_{t=1}^{T} W_t}$, and $\bar{t} = \frac{\sum_{t=1}^{T} W_t t}{\sum_{t=1}^{T} W_t}$.

The variance of the estimated ω:

$$\sigma_{\hat{\omega}}{}^2 = Var(\hat{\omega}) = Var\left[\frac{\sum_{t=1}^{T} W_t(t-\bar{t})y_t{}^\star}{\frac{1-\phi}{12}\sum_{t=1}^{T} W_t(t-\bar{t})^2}\right] = \frac{Var\left[\sum_{t=1}^{T} W_t(t-\bar{t})y_t{}^\star\right]}{(\frac{1-\phi}{12})^2\left[\sum_{t=1}^{T} W_t(t-\bar{t})^2\right]^2}$$

$$= \frac{Var\left[\sum_{t=1}^{T} W_t(t-\bar{t})\epsilon_t\right]}{(\frac{1-\phi}{12})^2\left[\sum_{t=1}^{T} W_t(t-\bar{t})^2\right]^2} = \frac{\sum_{t=1}^{T}[Var[W_t(t-\bar{t})\epsilon_t]]}{(\frac{1-\phi}{12})^2\left[\sum_{t=1}^{T} W_t(t-\bar{t})^2\right]^2}$$

$$= \frac{Var(\epsilon_t)\sum_{t=1}^{T} W_t{}^2(t-\bar{t})^2}{(\frac{1-\phi}{12})^2\left[\sum_{t=1}^{T} W_t(t-\bar{t})^2\right]^2} = \frac{\sigma_\epsilon{}^2\sum_{t=1}^{T} W_t{}^2(t-\bar{t})^2}{(\frac{1-\phi}{12})^2\left[\sum_{t=1}^{T} W_t(t-\bar{t})^2\right]^2} \quad (A8)$$

$$\sigma_{\hat{\omega}} = \frac{\sigma_\epsilon}{\frac{1-\phi}{12}}\frac{\sqrt{\sum_{t=1}^{T} W_t{}^2(t-\bar{t})^2}}{\sum_{t=1}^{T} W_t(t-\bar{t})^2} = \sigma_N g(T,\phi,W) \quad (A9)$$

$$g(T,\phi,W) = \sqrt{\frac{1+\phi}{1-\phi}}\frac{12\sqrt{\sum_{t=1}^{T} W_t{}^2(t-\bar{t})^2}}{\sum_{t=1}^{T} W_t(t-\bar{t})^2} \quad (A10)$$

Thus,

$$\sigma_{\hat{\omega}} = \sigma_N\sqrt{\frac{1+\phi}{1-\phi}}\frac{12\sqrt{\sum_{t=1}^{T} W_t{}^2(t-\bar{t})^2}}{\sum_{t=1}^{T} W_t(t-\bar{t})^2} \quad (A11)$$

From equation (A11), we conclude that the trend uncertainty is affected by the length of the available data, the natural variability in the data, the autocorrelation of the data and the weights.

A.3 Effect of measurement error

When we consider the instrumentation errors e_t in the measurements, Equation A2 becomes:

$$y_t = \mu + \omega X_t + N_t + e_t, t = 1,\cdots,T \quad (A12)$$

e_t is considered to be white noise with zero mean and common variance $\sigma_e{}^2$, $e_t \sim W(0,\sigma_e{}^2)$, and independent of N_t because N_t originates from unobserved or unsuspected atmospheric factors, while e_t comes from the instrument itself.

In this case, the variance of noise comes from two parts:

$$\sigma^2 = \sigma_N{}^2 + \sigma_e{}^2 \quad (A13)$$

Similar to the derivation in Equation (A9), the variance of the estimated trend magnitude is:

$$\begin{aligned}\sigma_{\hat{\omega}}{}^2 &= \sigma_N{}^2 g^2(T,\phi,W) + \sigma_e{}^2 g^2(T,0,W) \\ &= \sigma_N{}^2 \frac{1+\phi}{1-\phi}\frac{144\sum_{t=1}^{T} W_t{}^2(t-\bar{t})^2}{\left[\sum_{t=1}^{T} W_t(t-\bar{t})^2\right]^2} + \sigma_e{}^2 \frac{144\sum_{t=1}^{T} W_t{}^2(t-\bar{t})^2}{\left[\sum_{t=1}^{T} W_t(t-\bar{t})^2\right]^2} \\ &= \left(\sigma_N{}^2 \frac{1+\phi}{1-\phi} + \sigma_e{}^2\right)\frac{144\sum_{t=1}^{T} W_t{}^2(t-\bar{t})^2}{\left[\sum_{t=1}^{T} W_t(t-\bar{t})^2\right]^2}\end{aligned} \quad (A14)$$

The uncertainty of the all-sky radiance trend magnitude caused by the natural variability and the measurement error are shown in Figure A2b.

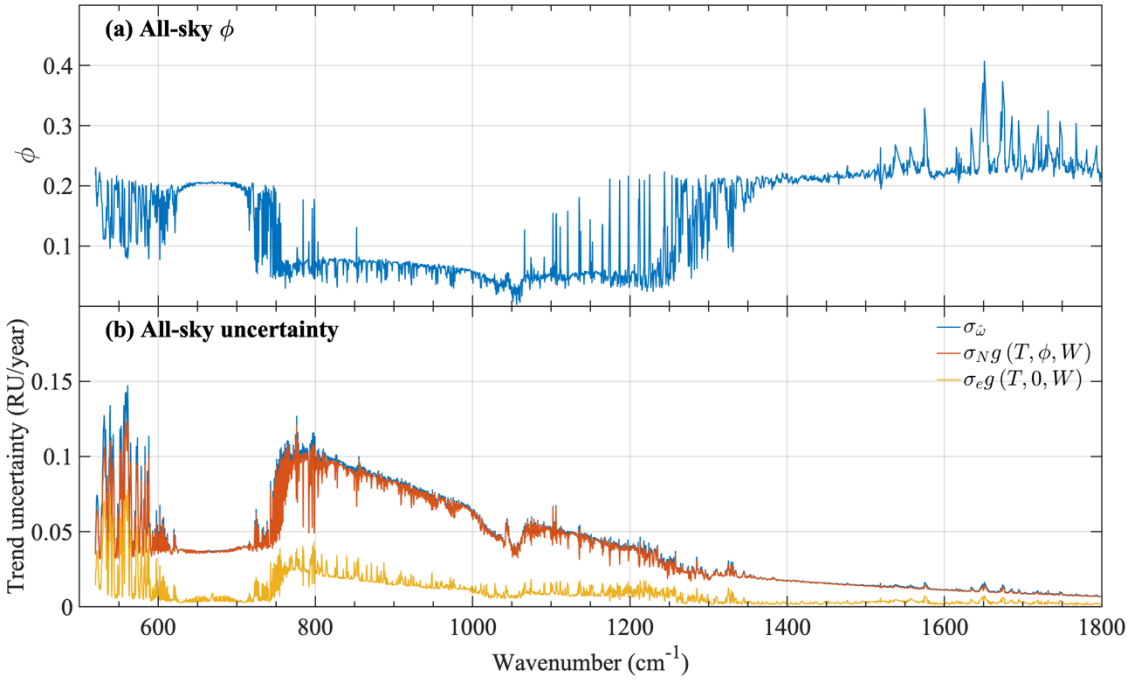

Figure A2. Parameters concerning the radiance trends. (a) The all-sky autocorrelation coefficient considering AR1 process; (b) All-sky DLR trend uncertainty decomposition based on Equation (A14). The blue line represents the total all-sky trend magnitude uncertainty. The orange and yellow lines represent the all-sky trend magnitude uncertainty arising from climate natural variability and measurement error respectively.

A.4 Time to detect the trend

The trend detection ω is judged to be real or significantly different from zero at the 5% level if $|\hat{\omega}| > 2\sigma_{\hat{\omega}}$. $\hat{\omega}$ is approximately normally distributed, so $z = \frac{\hat{\omega}-\omega}{\sigma_{\hat{\omega}}}$ follows a standard normal distribution.

$$Pr(|\hat{\omega}| > 2\sigma_{\hat{\omega}}) = Pr\left(z > 2 - \frac{\omega}{\sigma_{\hat{\omega}}}\right) \quad (A15)$$

To detect a real trend of specified magnitude $|\omega|$, with probability of 90%: $2 - \frac{\omega}{\sigma_{\hat{\omega}}} < -1.3 \Rightarrow \omega > 3.3\sigma_{\hat{\omega}}$.

Thus, the number of years $n^{\star}$ of data required to detect the trend $\hat{\omega}$ which is determined based on 23-year data:

551 $$n^{\star} \approx \frac{3.3\sigma_{\widehat{\omega}}}{|\widehat{\omega}|} \times 23\ years \qquad (A16)$$

552

553 **Appendix B: Homogenization of the two AERI records**

554 B.1 Comparison between the two AERIs

555 During the overlapping observation period, the all sky monthly mean radiance
556 difference between AERI-01 and AERI-C1 is shown in Figure B1. Since these two
557 instruments have different sampling frequency, the AERI-C1 spectra are averaged to match
558 the sampling of AERI-01 spectra before the comparison. From Figure B1a, there are
559 noticeable discrepancies between the AERI-01 and AERI-C1 observations. Because of the
560 different sampling frequency, the two AERIs have random errors of different amplitudes
561 (Turner et al., 2006). However, we find that removing the random errors using the principal
562 component analysis following Turner et al. (2006) has little impact on the discrepancies (not
563 shown). We find that in more than 20% of the AERI channels in the spectral range from 700
564 to 1300 cm^{-1} and for more than 12% of the overlapping observational months, the radiance
565 difference between two AERIs is larger than the documented absolute calibration uncertainty
566 (Knuteson et al., 2004a).

567 For AERI-C1 data stream, multiple instruments were used. All these transitions can
568 be seen in Figure B1a subtly or obviously. First, the transition from AERI-04 to AERI-05
569 happened in September 2009, which is subtly visible and is labelled by the green star in
570 Figure B1a. Next, in March 2010, the instrument changed from AERI-05 to AERI-06, which
571 is labelled by the green triangle in Figure B1a. Then, the transition from AERI-06 to AERI-
572 106 happened in March 2011, which is very obviously visible and is labelled by the green
573 square in Figure B1a. AERI-106 operated until July 2013 and was being replaced by AERI-
574 108 until present. It's interesting that the radiance differences between all of these "AERI-
575 C1" instruments and the AERI-01 have unique spectral signatures.

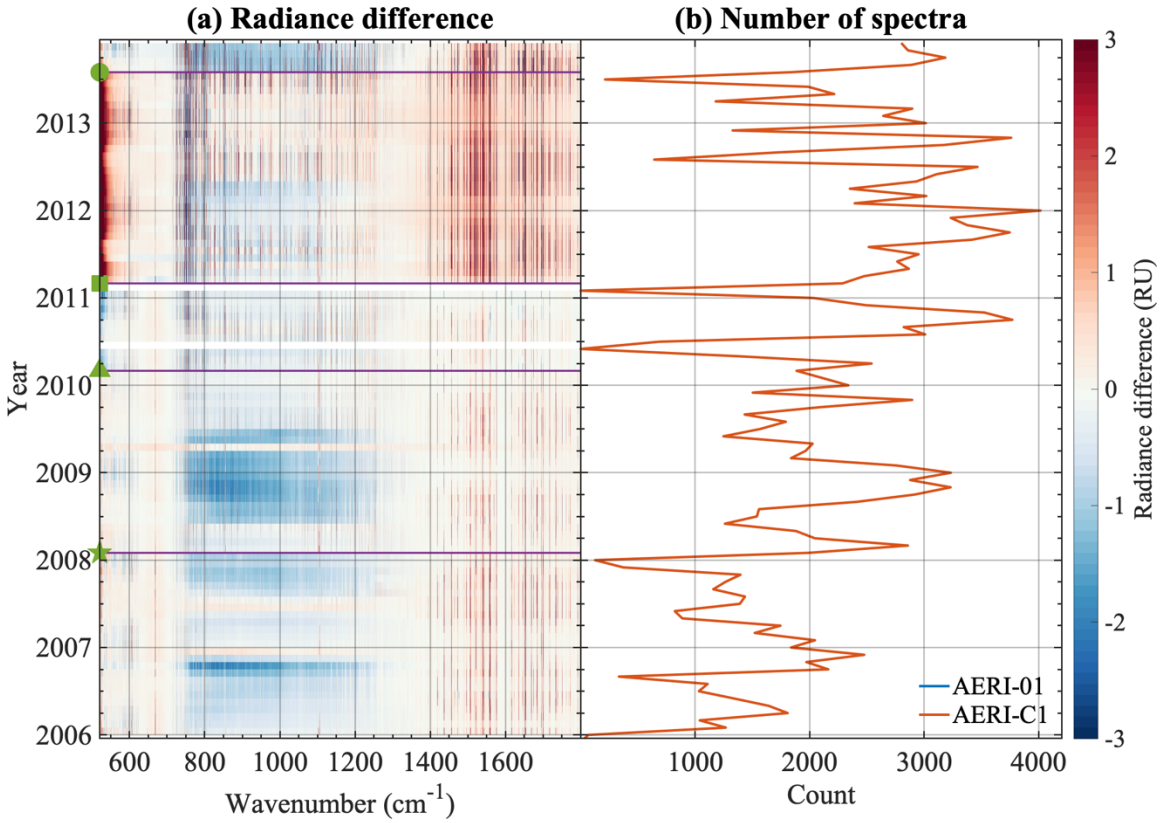

Figure B1. (a) The monthly mean DLR difference between AERI-C1 and AERI-01 (AERI-C1 – AERI-01). The green symbols mean the time of AERI-C1 instrument transition; (b) Number of 8-min spectra for each month (the counts are identical after AERI-C1 spectra are resampled to match AERI-01).

When separating the measured spectra to different sky types, we find that the prominent difference between the two AERIs in the window band mainly comes from relatively clear sky conditions. Figure B2 shows the monthly mean radiance difference for different sky types in October 2006 as an example. Here the DLR radiance at 985 cm^{-1} is used to classify the sky to be relatively clear (<40 RU) or relatively cloudy (>40 RU). We chose 40 RU based on the threshold that Turner and Gero (2011) used to classify cloudy sky to be thin or thick clouds scenes.

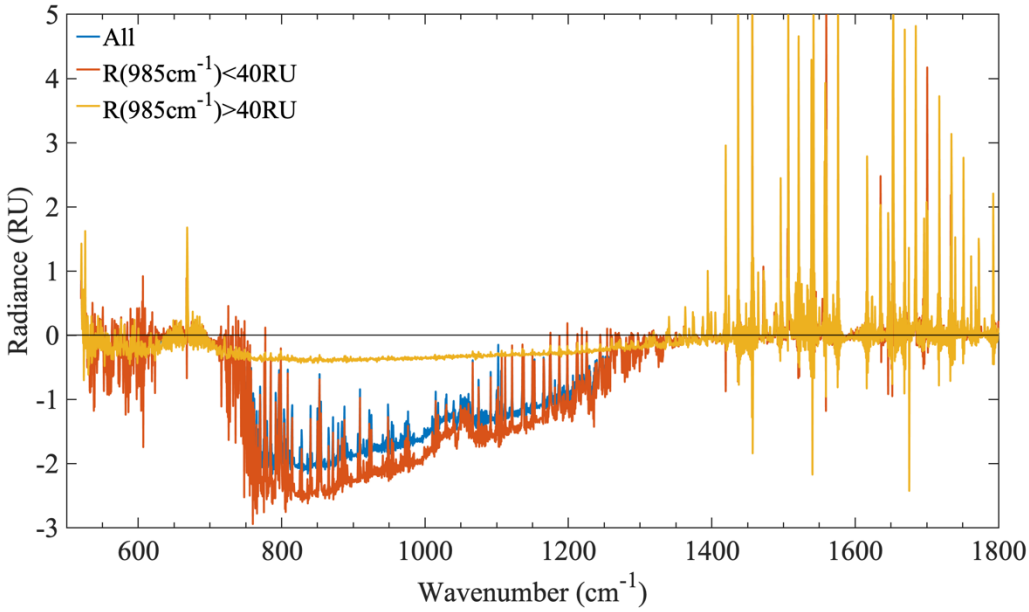

Figure B2. The monthly mean DLR difference between AERI-C1 and AERI-01 (AERI-C1 – AERI-01) for different sky conditions in October 2006

We examined various instrumental parameters recorded with AERI measurements, including calibration blackbody temperatures, instrument responsivity, and so on, but found that no instrumental parameter can indicate the radiance difference between the two AERIs.

B.2 Clear-sky LBLRTM simulations

Since the differences between two AERIs mainly come from relatively clear sky scenes, we use clear sky synthetic spectra simulated from LBLRTM as a metric to distinguish their relative accuracies. Here we use the classical backpropagation gradient-descent classification algorithm mentioned in Subsection 2.2 to select clear-sky spectra. To make sure the sky chosen is clear, we set the algorithm threshold to be 0.8, which means the possibility of the sky to be clear is at least 0.8.

After matching all datasets including radiosonde dataset and gas concentrations datasets at SGP mentioned in the Method section to select atmospheric profiles, clear sky synthetic spectra are obtained during the overlapping observational period. For each month, about 70 downwelling longwave spectra are simulated on average. The LBLRTM simulation is validated based on the test in Feldman et al. (2015). We chose the same time slices selected in Feldman et al. (2015) to simulate the DLR spectrum and we can achieve similar radiative closures between observation and simulation.

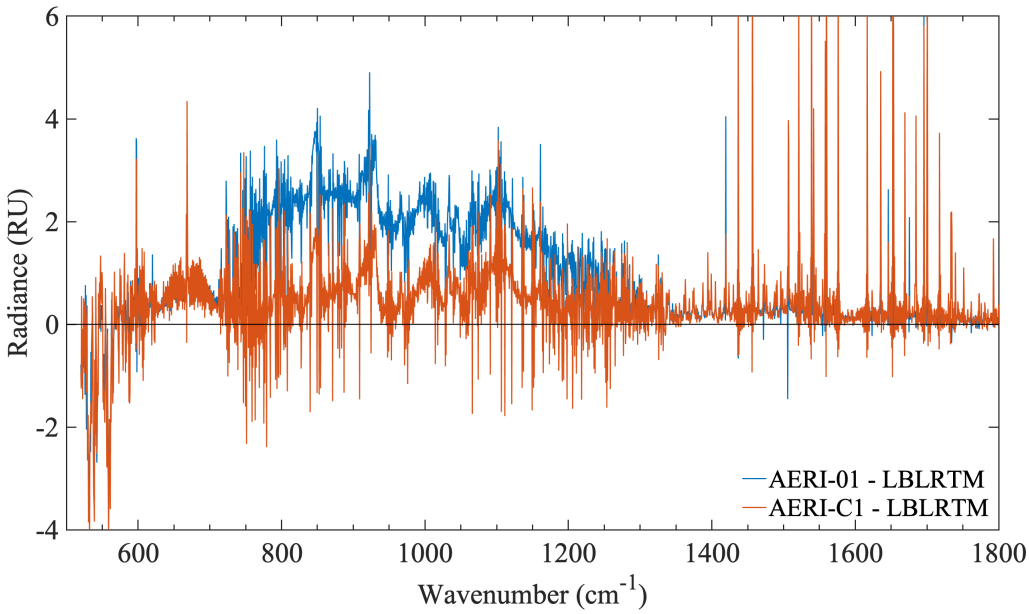

Figure B3. The clear sky monthly mean difference between AERI observations and LBLRTM simulations in October 2006.

We originally used the ozone concentration profile from the Modern-Era Retrospective analysis for Research and Applications Version 2 (MERRA-2, Gelaro et al., 2017) in simulating the synthetic spectra. A relatively poorer radiance closure between AERI observations and LBLRTM simulations was found in the ozone absorption band near 1040 cm^{-1}(not shown). By comparing to in situ measurements at SGP (available only at limited times), we find that this is due to poor representation of the local ozone concentration in the MERRA-2 dataset. To address this issue, we vertically scale the ozone profile uniformly to achieve an improved radiance closure in the ozone band as exemplified by Figure B3 (AERI-C1 line), although this has little impact on the all-sky radiance trend detected in Figure 5.

As exemplified in Figure B3, we find that AERI-C1 generally in better agreement with LBLRTM simulations than AERI-01 especially in the window band. The radiance difference in each channel is used to weight the spectra of AERI-01 and AERI-C1, according to Equation (2), to form an integrated record of monthly mean DLR radiance spectra.

References

Clough, S. A., Shephard, M. W., Mlawer, E. J., Delamere, J. S., Iacono, M. J., Cady-Pereira, K., Boukabara, S., & Brown, P. D. (2005). Atmospheric radiative transfer modeling: a summary of the AER codes. *Journal of Quantitative Spectroscopy and Radiative Transfer, 91*(2), 233-244. https://doi.org/10.1016/j.jqsrt.2004.05.058

Cunningham, P., & Delany, S. J. (2020). k-Nearest neighbour classifiers: (with Python examples). *arXiv preprint arXiv:2004.04523*.

Feldman, D. R., Collins, W. D., Gero, P. J., Torn, M. S., Mlawer, E. J., & Shippert, T. R.

(2015, Mar 19). Observational determination of surface radiative forcing by CO2 from 2000 to 2010. *Nature, 519*(7543), 339-343. https://doi.org/10.1038/nature14240

Gelaro, R., McCarty, W., Suárez, M. J., Todling, R., Molod, A., Takacs, L., Randles, C. A., Darmenov, A., Bosilovich, M. G., & Reichle, R. (2017). The modern-era retrospective analysis for research and applications, version 2 (MERRA-2). *Journal of Climate, 30*(14), 5419-5454.

Gero, P. J., & Turner, D. D. (2011). Long-Term Trends in Downwelling Spectral Infrared Radiance over the U.S. Southern Great Plains. *Journal of Climate, 24*(18), 4831-4843. https://doi.org/10.1175/2011jcli4210.1

Harries, J. E., Brindley, H. E., Sagoo, P. J., & Bantges, R. J. (2001). Increases in greenhouse forcing inferred from the outgoing longwave radiation spectra of the Earth in 1970 and 1997. *Nature, 410*(6826), 355-357.

Hersbach, H., Bell, B., Berrisford, P., Hirahara, S., Horányi, A., Muñoz-Sabater, J., Nicolas, J., Peubey, C., Radu, R., & Schepers, D. (2020). The ERA5 global reanalysis. *Quarterly Journal of the Royal Meteorological Society, 146*(730), 1999-2049.

Holdridge D. 2020. Balloon-Borne Sounding System (SONDE) Instrument Handbook. Ed. by Robert Stafford, U.S. Department of Energy. DOE/SC-ARM/TR-029.

Huang, Y. (2013). A simulated climatology of spectrally decomposed atmospheric infrared radiation. *Journal of Climate, 26*(5), 1702-1715.

Huang, Y., Chou, G., Xie, Y., & Soulard, N. (2019). Radiative control of the interannual variability of arctic sea ice. *Geophysical Research Letters, 46*(16), 9899-9908.

Huang, Y., Leroy, S. S., & Anderson, J. G. (2010). Determining longwave forcing and feedback using infrared spectra and GNSS radio occultation. *Journal of Climate, 23*(22), 6027-6035.

668 Huang, Y., & Ramaswamy, V. (2009). Evolution and Trend of the Outgoing Longwave
669 Radiation Spectrum. *Journal of Climate, 22*(17), 4637-4651.
670 https://doi.org/10.1175/2009jcli2874.1
671
672 Huang, Y., Ramaswamy, V., Huang, X., Fu, Q., & Bardeen, C. (2007). A strict test in climate
673 modeling with spectrally resolved radiances: GCM simulation versus AIRS
674 observations. *Geophysical Research Letters, 34*(24).
675 https://doi.org/10.1029/2007gl031409
676
677 Huang, Y., Ramaswamy, V., & Soden, B. (2007). An investigation of the sensitivity of the
678 clear-sky outgoing longwave radiation to atmospheric temperature and water vapor.
679 *Journal of Geophysical Research, 112*(D5). https://doi.org/10.1029/2005jd006906
680
681 Jacobson, A. R., Schuldt, K. N., Miller, J. B., Oda, T., Tans, P., Arlyn, A., Mund, J., Ott, L.,
682 Collatz, G. J., Aalto, T., Afshar, S., Aikin, K., Aoki, S., Apadula, F., Baier, B.,
683 Bergamaschi, P., Beyersdorf, A., Biraud, S. C., Bollenbacher, A., Bowling, D.,
684 Brailsford, G., Abshire, J. B., Chen, G., Huilin, C., Lukasz, C., Sites, C., Colomb, A.,
685 Conil, S., Cox, A., Cristofanelli, P., Cuevas, E., Curcoll, R., Sloop, C. D., Davis, K.,
686 Wekker, S. D., Delmotte, M., DiGangi, J. P., Dlugokencky, E., Ehleringer, J., Elkins,
687 J. W., Emmenegger, L., Fischer, M. L., Forster, G., Frumau, A., Galkowski, M., Gatti,
688 L. V., Gloor, E., Griffis, T., Hammer, S., Haszpra, L., Hatakka, J., Heliasz, M.,
689 Hensen, A., Hermanssen, O., Hintsa, E., Holst, J., Jaffe, D., Karion, A., Kawa, S. R.,
690 Keeling, R., Keronen, P., Kolari, P., Kominkova, K., Kort, E., Krummel, P., Kubistin,
691 D., Labuschagne, C., Langenfelds, R., Laurent, O., Laurila, T., Lauvaux, T., Law, B.,
692 Lee, J., Lehner, I., Leuenberger, M., Levin, I., Levula, J., Lin, J., Lindauer, M., Loh,
693 Z., Lopez, M., Luijkx, I. T., Myhre, C. L., Machida, T., Mammarella, I., Manca, G.,
694 Manning, A., Manning, A., Marek, M. V., Marklund, P., Martin, M. Y., Matsueda, H.,
695 McKain, K., Meijer, H., Meinhardt, F., Miles, N., Miller, C. E., Mölder, M., Montzka,
696 S., Moore, F., Josep-Anton, M., Morimoto, S., Munger, B., Jaroslaw, N., Newman, S.,
697 Nichol, S., Niwa, Y., O'Doherty, S., Mikaell, O.-L., Paplawsky, B., Peischl, J., Peltola,
698 O., Jean-Marc, P., Piper, S., Plass-Dölmer, C., Ramonet, M., Reyes-Sanchez, E.,
699 Richardson, S., Riris, H., Ryerson, T., Saito, K., Sargent, M., Sasakawa, M., Sawa, Y.,
700 Say, D., Scheeren, B., Schmidt, M., Schmidt, A., Schumacher, M., Shepson, P.,

701 Shook, M., Stanley, K., Steinbacher, M., Stephens, B., Sweeney, C., Thoning, K.,
702 Torn, M., Turnbull, J., Tørseth, K., Bulk, P. V. D., Dinther, D. V., Vermeulen, A.,
703 Viner, B., Vitkova, G., Walker, S., Weyrauch, D., Wofsy, S., Worthy, D., Dickon, Y., &
704 Miroslaw, Z. (2020). *CarbonTracker CT2019B*.
705 https://www.esrl.noaa.gov/gmd/ccgg/carbontracker/CT2019B/
706
707 Kapsch, M.-L., Graversen, R. G., Tjernström, M., & Bintanja, R. (2016). The effect of
708 downwelling longwave and shortwave radiation on Arctic summer sea ice. *Journal of*
709 *Climate, 29*(3), 1143-1159.
710
711 Knuteson, R., Revercomb, H., Best, F., Ciganovich, N., Dedecker, R., Dirkx, T., Ellington, S.,
712 Feltz, W., Garcia, R., & Howell, H. (2004a). Atmospheric emitted radiance
713 interferometer. Part I: Instrument design. *Journal of Atmospheric and Oceanic*
714 *Technology, 21*(12), 1763-1776.
715
716 Knuteson, R., Revercomb, H., Best, F., Ciganovich, N., Dedecker, R., Dirkx, T., Ellington, S.,
717 Feltz, W., Garcia, R., & Howell, H. (2004b). Atmospheric emitted radiance
718 interferometer. Part II: Instrument performance. *Journal of Atmospheric and Oceanic*
719 *Technology, 21*(12), 1777-1789.
720
721 Liebmann, B., & Smith, C. A. (1996). Description of a complete (interpolated) outgoing
722 longwave radiation dataset. *Bulletin of the American Meteorological Society, 77*(6),
723 1275-1277.
724
725 Lubin, D. (1994). The role of the tropical super greenhouse effect in heating the ocean
726 surface. *Science, 265*(5169), 224-227.
727
728 Peters, W., Jacobson, A. R., Sweeney, C., Andrews, A. E., Conway, T. J., Masarie, K., Miller,
729 J. B., Bruhwiler, L. M., Pétron, G., & Hirsch, A. I. (2007). An atmospheric
730 perspective on North American carbon dioxide exchange: CarbonTracker.
731 *Proceedings of the National Academy of Sciences, 104*(48), 18925-18930.
732
733 Revercomb, H. E., Buijs, H., Howell, H. B., LaPorte, D. D., Smith, W. L., & Sromovsky, L.

(1988). Radiometric calibration of IR Fourier transform spectrometers: solution to a problem with the High-Resolution Interferometer Sounder. *Applied Optics, 27*(15), 3210-3218.

Revercomb, H. E., Turner, D. D., Tobin, D., Knuteson, R. O., Feltz, W., Barnard, J., Bösenberg, J., Clough, S., Cook, D., & Ferrare, R. (2003). The ARM program's water vapor intensive observation periods: Overview, initial accomplishments, and future challenges. *Bulletin of the American Meteorological Society, 84*(2), 217-236.

Rowe, P. M., Neshyba, S. P., Cox, C. J., & Walden, V. P. (2011). A responsivity-based criterion for accurate calibration of FTIR emission spectra: identification of in-band low-responsivity wavenumbers. *Optics express, 19*(7), 5930-5941.

Rowe, P. M., Neshyba, S. P., & Walden, V. P. (2011). Responsivity-based criterion for accurate calibration of FTIR emission spectra: theoretical development and bandwidth estimation. *Optics express, 19*(6), 5451-5463.

Shupe, M. D., & Intrieri, J. M. (2004). Cloud Radiative Forcing of the Arctic Surface: The Influence of Cloud Properties, Surface Albedo, and Solar Zenith Angle. *Journal of Climate, 17*(3), 616-628. https://doi.org/10.1175/1520-0442(2004)017<0616:Crfota>2.0.Co;2

Sokolowsky, G. A., Clothiaux, E. E., Baggett, C. F., Lee, S., Feldstein, S. B., Eloranta, E. W., Cadeddu, M. P., Bharadwaj, N., & Johnson, K. L. (2020). Contributions to the Surface Downwelling Longwave Irradiance during Arctic Winter at Utqiaġvik (Barrow), Alaska. *Journal of Climate, 33*(11), 4555-4577. https://doi.org/10.1175/jcli-d-18-0876.1

Stephens, G. L., Li, J., Wild, M., Clayson, C. A., Loeb, N., Kato, S., L'Ecuyer, T., Stackhouse, P. W., Lebsock, M., & Andrews, T. (2012). An update on Earth's energy balance in light of the latest global observations. *Nature Geoscience, 5*(10), 691-696. https://doi.org/10.1038/ngeo1580

767 Tiao, G. C., Reinsel, G. C., Xu, D., Pedrick, J., Zhu, X., Miller, A., DeLuisi, J., Mateer, C., &
768 Wuebbles, D. (1990). Effects of autocorrelation and temporal sampling schemes on
769 estimates of trend and spatial correlation. *Journal of Geophysical Research:*
770 *Atmospheres, 95*(D12), 20507-20517.
771
772 Trenberth, K. E., Fasullo, J. T., & Kiehl, J. (2009). Earth's Global Energy Budget. *Bulletin of*
773 *the American Meteorological Society, 90*(3), 311-324.
774 https://doi.org/10.1175/2008bams2634.1
775
776 Turner, D., Knuteson, R., Revercomb, H., Lo, C., & Dedecker, R. (2006). Noise reduction of
777 Atmospheric Emitted Radiance Interferometer (AERI) observations using principal
778 component analysis. *Journal of Atmospheric and Oceanic Technology, 23*(9), 1223-
779 1238.
780
781 Turner, D. D., & Gero, P. J. (2011). Downwelling 10μm radiance temperature climatology for
782 the Atmospheric Radiation Measurement Southern Great Plains site. *Journal of*
783 *Geophysical Research, 116*(D8). https://doi.org/10.1029/2010jd015135
784
785 Turner, D. D., Lesht, B. M., Clough, S. A., Liljegren, J. C., Revercomb, H. E., & Tobin, D.
786 (2003). Dry bias and variability in Vaisala RS80-H radiosondes: The ARM
787 experience. *Journal of Atmospheric and Oceanic Technology, 20*(1), 117-132.
788
789 Turner, D. D., Tobin, D., Clough, S. A., Brown, P. D., Ellingson, R. G., Mlawer, E. J.,
790 Knuteson, R. O., Revercomb, H. E., Shippert, T. R., & Smith, W. L. (2004). The QME
791 AERI LBLRTM: A closure experiment for downwelling high spectral resolution
792 infrared radiance. *Journal of the atmospheric sciences, 61*(22), 2657-2675.
793
794 Wang, J., Cole, H. L., Carlson, D. J., Miller, E. R., Beierle, K., Paukkunen, A., & Laine, T. K.
795 (2002). Corrections of humidity measurement errors from the Vaisala RS80
796 radiosonde—Application to TOGA COARE data. *Journal of Atmospheric and*
797 *Oceanic Technology, 19*(7), 981-1002.
798
799 Weatherhead, E. C., Reinsel, G. C., Tiao, G. C., Meng, X.-L., Choi, D., Cheang, W.-K.,

Keller, T., DeLuisi, J., Wuebbles, D. J., Kerr, J. B., Miller, A. J., Oltmans, S. J., & Frederick, J. E. (1998). Factors affecting the detection of trends: Statistical considerations and applications to environmental data. *Journal of Geophysical Research: Atmospheres, 103*(D14), 17149-17161. https://doi.org/10.1029/98jd00995

Wielicki, B. A., Wong, T., Allan, R. P., Slingo, A., Kiehl, J. T., Soden, B. J., Gordon, C., Miller, A. J., Yang, S.-K., & Randall, D. A. (2002). Evidence for large decadal variability in the tropical mean radiative energy budget. *Science, 295*(5556), 841-844.

Wild, M., Folini, D., Schär, C., Loeb, N., Dutton, E. G., & König-Langlo, G. (2012). The global energy balance from a surface perspective. *Climate Dynamics, 40*(11-12), 3107-3134. https://doi.org/10.1007/s00382-012-1569-8